energies

MDPI

Article

Experimental Study on Heuristics Energy Management Strategy for Hybrid Energy Storage System

Alok Ranjan [1,*], Sanjay Bodkhe [1], Gaurav Goyal [1], Archana Belge [2] and Sneha Tibude [1]

[1] Department of Electrical Engineering, Shri Ramdeobaba College of Engineering and Management, Nagpur 440013, India; bodkhesb@rknec.edu (S.B.); goyalg@rknec.edu (G.G.); tibudesb@rknec.edu (S.T.)
[2] Department of Mechanical and Mechatronics Engineering, Thakur College of Engineering and Technology, Mumbai 400101, India; archanabelge2@gmail.com
* Correspondence: ranjana_1@rknec.edu

Abstract: The energy management strategy (EMS) is a decision-making algorithm for effective power allocation between storage devices in a hybrid energy storage system (HESS). Source voltages, state of charge (SOC), the terminal voltage of the load, and the rate of change in the battery current must be considered while implementing the EMS and, hence, they are termed as performance indicators. This research work focuses on the development of an EMS, designed to manage the performance indicators of the sources (terminal voltage and battery current rate) and ensure efficient power distribution through a shared bus topology. A shared bus topology employs individual converters for each source, offering efficient control over these sources. Rule-based fuzzy logic control ensures efficient power distribution between batteries and ultracapacitors. Additionally, hardware has been developed to validate the power allocation strategy and regulate the DC-link voltage in the energy management system (EMS). dSPACE MicroLabBox is utilized for the implementation of real-time control strategies. A battery and an ultracapacitor bank are utilized in a hybrid energy storage system. The simulation outcomes have been corroborated by experimental data, affirming the efficacy of the proposed energy management strategy. The proposed EMS achieves a 2.1% battery energy saving compared to a conventional battery electric vehicle over a 25 s duration under the same load conditions.

Keywords: battery; energy management strategy; energy storage; ultracapacitor

Citation: Ranjan, A.; Bodkhe, S.; Goyal, G.; Belge, A.; Tibude, S. Experimental Study on Heuristics Energy Management Strategy for Hybrid Energy Storage System. *Energies* **2024**, *17*, 5850. https://doi.org/10.3390/en17235850

Academic Editors: Namwook Kim and Heeyun Lee

Received: 10 October 2024
Revised: 10 November 2024
Accepted: 16 November 2024
Published: 22 November 2024

1. Introduction

The energy and power densities of a source are responsible for the effective performance of a standalone load that is not connected to the grid [1]. For example, in a battery electric vehicle (BEV), the battery suffers from many short-term transients that require colossal power [2–4]. Being a single source and due to these transients, the battery's performance gets degraded during long-term operation [5,6]. This is similar to the gradual decline in performance of fuel cell-based vehicles. The performance degradation not only affects efficiency and output power but also shortens the service life and increases maintenance costs. Therefore in a single source system, accurate prediction of the performance degradation of the source should be carried out [7,8]. For lithium batteries, identifying the health condition of the battery is equally important because the microhealth parameter, which reflects the performance of active material and electrolytes inside the battery, portrays the battery's internal health state. Any change in the microhealth parameters can be identified with the help of a simplified P2D model [9]. Wherever a fuel cell stack is used in an electric vehicle or hybrid electric vehicle, a degradation adaptive energy management strategy can be used to keep the output of the powertrain optimal all the time [10]. One more parameter of the battery called the state of charge (SOC) significantly influences energy management. To accurately determine the SOC, nondestructive techniques, like SOC estimation based on ultrasonic reflection waves, can be employed [11]. In studies, multiple storage is identified

as a reliable alternative to safeguard the battery. Ultracapacitor (UC) technology is one of the best hybridization sources due to its favorable properties [12–17].

Energy storage plays a crucial role in power systems and electric transportation, making the optimization of these storage systems essential. Volterra equations have become a valuable tool for modeling and analyzing energy storage integrated with renewable energy sources. Using Volterra equations, dynamic analyses of energy storage combined with renewable and diesel generation have been conducted [18]. Additionally, a mathematical model for battery energy storage systems is implemented using Volterra equations [19]. The Volterra integral equation, particularly the first kind, is effective in capturing nonlinear behavior.

To control the power transaction between the sources and the load, various EMSs are reported in the research as rule based and optimization based. Being simple in nature, easily understandable, and real-time implementable, the rule-based EMS is preferred widely [20–23]. A review of intelligent energy management systems for electrified vehicles is discussed in [20], where characteristics of rule-based EMSs are discussed. In [21], a novel rule-based approach has been devised to achieve an effective power balance between the battery and supercapacitor. The supercapacitor is in a charged state at the end of each cycle in this method. The on-board transaction strategy is discussed in [22]. Reference [23] shows how a rule-based EMS can be applied to solar, fuel cell, and biomass energy storage systems. Classical EMSs are widely available in the work [16,24–26]. DC-link voltage regulation is considered a prime controlling factor in microgrid systems in [16]. UC voltage and battery current rate regulation are taken as essential criteria in [24]. In [25], a diesel generator, a battery, and a photovoltaic system are utilized as HESS to provide power supply in critical circumstances. The management of the energy is dependent on a fuzzy rules-based EMS. Multiple sources like batteries, UC, photovoltaic (PVs) panels, and fuel cells (FCs) and their integration in a specific manner are discussed in [27] with a power tracking control mechanism. For a battery UC hybrid energy storage system (HESS), a control algorithm based on energy is shown in [28] for a grid system. Reference [29] has demonstrated that the UC's SOC is a controlling factor for generating the battery's reference current. Fuzzy logic controllers are also reported for controlling UC voltage, battery peak power, power allocation, and energy level handling [30–32].

The way of interconnection between the battery and UC decides the topologies. These topologies are important in regulating the source parameters. A comparative study is conducted to determine the optimal architecture and converter topology for an HESS in a solar-powered DC microgrid [33]. Power converter topologies for energy storage systems include isolated and non-isolated converters. HESS architectures are categorized as passive, semi-active, fully active, and multi-level HESSs. A passive topology lacks any control over performance indicators as converters are absent [34]. In a semi-active topology, only one converter is utilized, and the performance indicators of the other source remain uncontrolled. This strategy increases the current of the controlled source. In this strategy, the current of the controlled source increases [35]. Cascade topology is also employed to enhance battery life. However, as a series connection, the control is intricate, and frequent charging of the UC is necessary [36]. Multiport topologies have been developed that are both compact and complex, capable of utilizing multiple sources [37,38]. The existing and proposed topologies are compared and discussed in [39]. The shared bus topology is widely used to control performance indicators because it employs individual converters for the sources, making the control process straightforward [40,41].

Rule-based EMSs suffer in pinpoint power distribution, but they ease real-time implementation. Optimization-based EMSs overcome this limitation, but their real-time implementation is complex. Also, limited work is verified through hardware development. In [34], a review of different EMSs is discussed. The conventional and modified rule-based EMS (MRB-EMS) is shown in [42,43] with DC-link voltage compensation. Accurate power allocation with a fuzzy logic controller is discussed in [44].

In this experimental study, a fuzzy logic-based EMS is crucial for efficient power distribution among sources. To protect the battery from peak power demands, a battery

current rate limiter is utilized. Additionally, DC-link voltage regulation ensures effective load control. A hardware setup is developed with the help of the dSPACE MicroLabBox controller, converters, sources, level shifters, driver circuits, and sensors. Two different modes of the power-sharing strategy are examined here. These modes are low- and high-power demand modes. DC-link voltage or load voltage is regulated to 48 V, irrespective of load power variations. The results analyzed after a detailed experimental study concur with the simulation results and confirm the effectiveness of the proposed power allocation strategy.

This work is organized as follows. The circuit topology and its operation are discussed in Section 2. Section 3 gives an overview of the EMS and its development. The component design and selection of ratings are shown in Section 4. The experimental setup and its discussion are given in Section 5. Performance analysis is detailed in Section 6, while Section 7 contains the conclusion.

2. Topology and Modes of Operation

The performance indicators are effectively controlled by shared bus topology. They consist of a boost and one bi-directional dc-dc converter. The boost converter controls the power flow between the battery and the load, whereas the bi-directional converter controls the power transaction between the UC and the load. The circuit topologies are shown in Figures 1 and 2. The working patterns of the switches Q_1, Q_2, and Q_0 decide their modes of operation. For experimental study purposes, two modes are explored and studied.

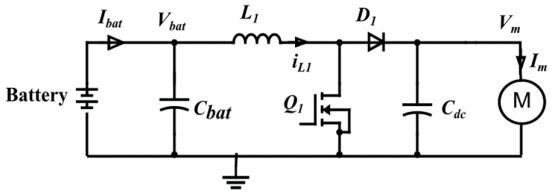

Figure 1. Battery-boost converter for LPDM.

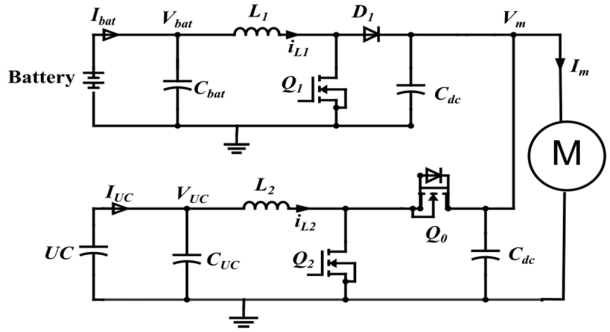

Figure 2. Shared bus topology for HPDM.

2.1. Mode I—Low-Power Demand Mode (LPDM)

In this mode, the required load power is less than the base power. The battery alone is sufficient to tackle the load requirement. After analyzing the complete power profile, the base power is defined. The base power should be such that the battery should be able to provide it easily. It is a transient-free power. The circuit configuration for LPDM is shown in Figure 1. It shows the battery voltage (V_{bat}), battery current (I_{bat}), load voltage (V_m), load current (I_m), input capacitor (C_{bat}), inductor (L_1), inductor current (i_{L1}), switch (Q_1), diode (D_1), and DC-link capacitor (C_{dc}), which are all related to the boost converter circuit.

The expression for the load voltage for this mode is given by Equation (1).

$$V_m(t) = \frac{1}{C_{dc}} \int i_{L1}(t)dt \tag{1}$$

2.2. Mode II—High-Power Demand Mode (HPDM)

In this mode, the power required by the load is more than the base power. This additional requirement of power is fulfilled by the UC bank. Figure 2 illustrates the circuit configuration used in this operational mode. It shows the UC voltage (V_{UC}), UC current (I_{UC}), input capacitor (C_{UC}), inductor (L_2), inductor current (i_{L2}), and switches (Q_2 and Q_0), which are all related to the bi-directional converter circuit. d_{Q1} and d_{Q2} are the duty ratios of the two pulses generated for Q_1 and Q_2 switches, respectively. In this mode, both converters operate together to provide the required power to the load.

Equations (2)–(6) illustrate the functioning of this operational mode. Here, two pulses are generated for switches Q_1 and Q_2 simultaneously for the operation.

The load voltage (V_m) for both converters is given by Equation (2). d_{Q1} and d_{Q2} are the duty ratios for both converters in boost mode.

$$V_m = \frac{V_{bat}}{1 - d_{Q1}} = \frac{V_{UC}}{1 - d_{Q2}} \tag{2}$$

Load current $i_m(t)$ is the summation of the inductor currents and is given by Equation (3).

$$i_m(t) = i_{L1}(t) + i_{L2}(t) \tag{3}$$

The expression for inductor currents $i_{L1}(t)$ and $i_{L2}(t)$ is given by Equations (4) and (5).

$$i_{L1}(t) = \frac{1}{L_1} \int v_{bat}(t) d_{Q1} dt \tag{4}$$

$$i_{L2}(t) = \frac{1}{L_2} \int v_{UC}(t) d_{Q2} dt \tag{5}$$

The load voltage ($v_m(t)$) in the time domain is given by Equation (6). C_{dc} is the DC-link capacitor.

$$v_m(t) = \frac{1}{C_{dc}} \int (i_{L1}(t) + i_{L2}(t)) dt \tag{6}$$

3. Energy Management Strategy

A modified energy management system (EMS) designed for enhanced control over performance indicators is discussed in [39]. A fuzzy logic controller is used to allocate the power between the battery and UC. The Sugeno fuzzy logic controller is designed for precise power allocation, working with the base power and high power. Inputs are the required load power (P_m) and the output is battery power (P_{bat}). With a base power of 70 watts, if the load requirement is below 70 watts (true condition), the output is the required load power. If the load requirement exceeds 70 watts (high condition), the output remains at 70 watts. The control strategy, outlined in Table 1, operates within a range of 0 to +100 watts, with its effectiveness demonstrated in Figure 3.

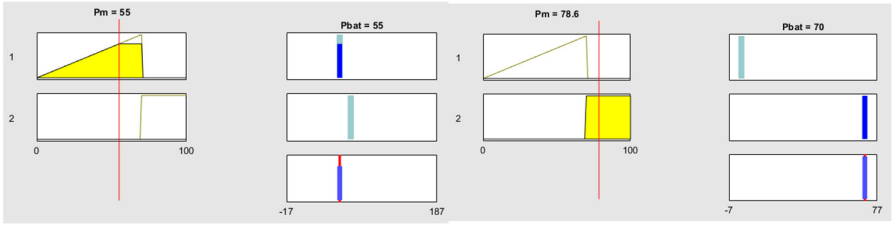

(**a**) (**b**)

Figure 3. Rule viewer for the fuzzy logic control strategy (**a**) for LPDM (**b**) for HPDM.

In this experimental study, DC-link voltage regulation, power allocation, and rate limiter functionality are the main focus of the investigation. The control strategy used for the experimental verification is shown in Figure 4.

Table 1. Control strategy for the fuzzy logic controller.

$P_m \backslash P_{bat}$	High	Right
B_p	0	True
H_p	B_p	B_p

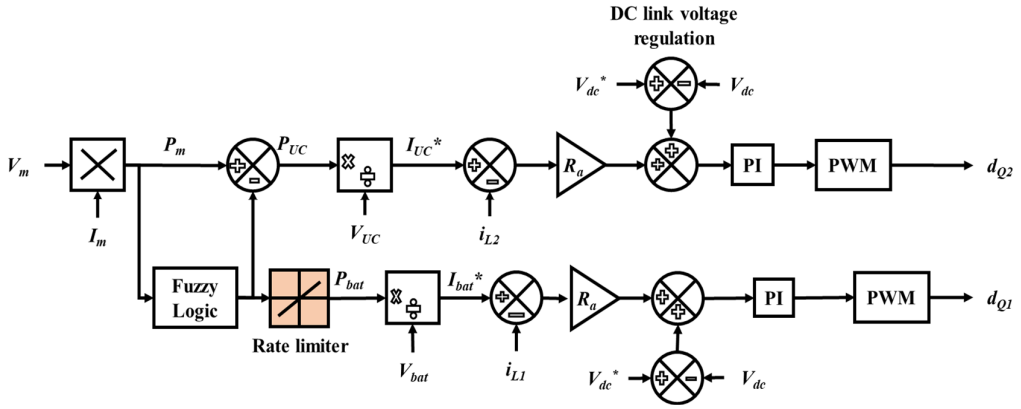

Figure 4. Control strategy for a modified EMS with a rate limiter.

The total load power (P_m) is calculated from load voltage (V_m) and load current (I_m). The fuzzy logic controller allocates power commands to the battery (P_{bat}). The UC power (P_{UC}) allocation is obtained from load and battery power. Based on P_{bat} and P_{UC}, current signals $I_{bat}{}^*$ and $I_{UC}{}^*$ are generated by dividing the power by voltages. Errors in battery and UC current are generated by the difference between i_{L1} and i_{L2}. The resistance R_a converts the error signal into a voltage signal. A DC-link voltage compensation loop regulates the voltage at a constant value of 48 V. $V_{dc}{}^*$ is taken as reference DC-link voltage. V_{dc} is the generated DC-link voltage. PI controllers minimize the error, which helps in effective PWM pulse generation for switches Q_1 and Q_2. The rate limiter performs its function well and limits the high rise of the battery current.

The high rising rate of the battery current degrades the battery's performance. In research, experiments are performed on lithium batteries with a high discharging current rate, and its impact is noticed. An 83 C discharging current was imposed on a 3 Ah lithium battery, while standard discharge was 1 C. As a result, after 400 cycles, it was found that a 20% reduction in capacity occurred along with a reduction in battery life [45]. Another experiment on lithium-ion phosphate batteries had a 2.6 Ah capacity and a standard discharge rate of 1 C. The pulsed discharging current imposed was 10.8 C. After 700 cycles, 22.8% of capacity was reduced, and the life cycle was reduced by 38%. So, in this experiment, the implemented rate limiter protects the battery from a high current rate. The rising rate used is 100 watts/s based on [39].

Expressions involved in generating gate pulses for the power switches are shown in Equation (7) as follows:

The battery power (P_{bat}) is given by

$$P_{bat} = rate \times fuzzyLogicOutput \tag{7}$$

where $rate = \frac{U(P_{bat}) - Y(P_{bat}-1)}{t(P_{bat}) - t(P_{bat}-1)}$.

The battery power at the current step is $U(P_{bat})$ with respect to time $t(P_{bat})$. $Y(P_{bat}-1)$ is the battery power in the previous step with time $t(P_{bat}-1)$. The steps involved in calculating the rate are power and time in the initial and previous stages. These steps decide whether the slew rate is rising or falling.

The output $Y(P_{bat})$ is based on Equations (8) and (9). The rising slew rate (R) and falling slew rate (F) decide the output nature. The sample time is Δt.

$$Y(P_{bat}) = \Delta t \times R + Y(P_{bat} - 1); \text{rate} > \text{R} \quad (8)$$

$$Y(P_{bat}) = \Delta t \times F + Y(P_{bat} - 1); \text{rate} > \text{R} \quad (9)$$

Gate pulse d_{Q1} for switch Q_1 is given by Equation (10).

$$d_{Q1} = PWM \times k_p \left\{ \left(\frac{P_{bat}}{V_{bat}} - i_{L1} \right) R_a + (48 - V_m) \right\} dt + k_i \int \{ (\frac{P_{bat}}{V_{bat}} - i_{L1}) R_a + (48 - V_m) \} dt \quad (10)$$

The k_p and k_i values are 0.008 and 0.001, respectively.

Equation (11) represents the gate pulse for switch Q_2.

$$d_{Q2} = PWM \times k_p \{ \left(\frac{P_{UC}}{V_{UC}} - i_{L2} \right) R_a + (48 - V_m) \} dt + k_i \int \{ (\frac{P_{UC}}{V_{UC}} - i_{L2}) R_a + (48 - V_m) \} dt \quad (11)$$

The k_p and k_i values for gate pulse d_{Q2} are 0.1 and 0.01, respectively.

The expression of energy with respect to time ($E_n(t)$) is given by Equation (12). This expression is used to calculate the total energy transfer and percentage of energy saved.

$$E_n(t) = \int V_{bat}(t) \times I_{bat}(t) dt \quad (12)$$

4. Rating Selection and Design

4.1. Selection of Battery Rating

Equation (12) provides the energy requirement of the load. The battery should be able to deliver this energy requirement for a load running at 48 V with current 25 A for 1.5 h; the energy required will be 1.8 kWh. To meet this requirement, the selected battery rating is 24 V and 100 Ah. This battery has a nominal voltage of 25.6 V, with a maximum discharge current of 80 A and a continuous discharge current of 50 A. The maximum charging current is 25 A. The charge cutoff voltage is 28.8 V, while the discharge cutoff voltage is 22.4 V. It operates efficiently within a temperature range of −10 °C to +45 °C and boasts a cycle life of over 2000 cycles.

4.2. UC Rating Selection

The UC is used to protect the battery during peak power demand mode. This UC should drive and accept the energy from the load.

The rating of the UC is calculated based on total energy required (W_{UC}) and is tabulated in Table 2.

Table 2. UC specifications.

Parameters	Rating	Parameters	Rating
Single-cell rating	2.7 V, 500 F.	Main UC	24.3 V, 55.55 F
Total cells	9	Capacity	kJ

4.3. Converter Rating Selection

Converters are the medium of power exchange. A well-designed converter provides better efficiency. The converter component rating selection is performed by Equations (13)–(17) [46].

The duty cycle for both the boost converters is given by Equation (13).

$$D = 1 - \frac{V_{in\_min} \times \eta_c}{V_{Out}} \quad (13)$$

D is the duty cycle, V_{in_min} is the minimum input voltage, V_{Out} is the desired output voltage, and η_c is the converter efficiency.

The ripple current for the inductors (ΔI_L) is given by Equation (14). A good estimation of the inductor current is 20% to 40% of the output current.

$$\Delta I_L = \frac{V_{in\_min} \times D}{f_s \times L} \tag{14}$$

f_s is the switching frequency of the converter. L is the selected inductor rating.
For a good estimation of the inductor value, Equation (15) is applicable.

$$\mathrm{L} = \frac{V_{in} \times (V_{out} - V_{in})}{\Delta \mathrm{I}_L \times f_s \times V_{out}} \tag{15}$$

V_{in} is the typical input voltage and V_{out} is the desired output voltage.
The maximum output current (I_{out_max}) that can be delivered is given by Equation (16).

$$I_{out\_max} = (I_{LIM\_min} - \frac{\Delta I_L}{2}) \times (1 - D) \tag{16}$$

I_{LIM_min} is the minimum value current limit of the switch.
The minimum value of the output capacitor ($C_{out_{min}}$) can be calculated by Equation (17). ΔV_{out} is the ripple voltage.

$$C_{out_{min}} = \frac{I_{out\_max} \times D}{f_s \times \Delta V_{out}} \tag{17}$$

The input capacitance for the battery and UC are C_{UC} and C_{bat}, respectively. f_s is the switching frequency. The parameters of the converter are shown in Table 3. The inductor value is taken as 1.5 mH and the input capacitor as 1200 µF. The value of the output capacitor is 1200 µF.

Table 3. Converter specifications.

Parameters	Values	Parameters	Values
Minimum input voltage (V_{in_min})	24 V.	Current ripple (Δi_{L2})	20% of I_a
Load voltage (V_m)	48 V.	Voltage ripple (ΔV_m)	±2%
Converter efficiency (η_c)	80%.	Load resistance (R_a)	2.5 Ohm
Switching period (T_s)	1/10,000 s	C_{UC}	1200 µF
Rated motor current (I_m)	25 A.	(C_{bat})	1200 µF
DC-link voltage (V_{dc})	48 V.	Boost converter inductor (L_1)	14.44 µH
Bi-directional converter inductor (L_2)	40.32 µH.	Switching frequency (f_s)	10 kHz

5. Experimental Setup

For experimental verification, dSPACE MicroLabBox (dSPACE, Paderborn, Germany) is used as a controller. MicroLabBox is a rapid control prototyping unit used for quickly developing and testing control strategies. It features an NXP QorIQ P5020 dual-core 2 GHz processor, 1 GB of dynamic random-access memory (DRAM), and 128 MB of flash memory. The unit also offers over 100 input–output channels, which include an analog input channel, analog output, digital input and output, a serial interface, and electric motor control capabilities [47]. The complete experimental setup is shown in Figure 5. Six analog signals (load voltage and current, battery voltage and battery-boost inductor current, UC voltage, and UC bi-directional inductor current) are used to develop the EMS for the converters in the real-time interface with dSPACE MicroLabBox. Two digital output pulses are developed for the triggering of converter modules. These two digital pulses have a level of 3.3 V, but for the triggering of IGBT, the pulse level should be 15 V. A level shifter shifts the pulse level from 3.3 V to 15 V. The level shifter is powered by 20 V AC, which is provided by a 20-0-20 single-phase step-down transformer.

The analog input pin interface of the controller is used to develop the control strategy in a real-time environment for the converters. A voltage sensor and a current sensor are

used to measure the load voltage (V_m) and load current (I_m) to determine the load power (P_m) requirement. The fuzzy logic controller then distributes this load between the battery and the ultracapacitor. Two voltage sensors monitor the battery voltage (V_{bat}) and UC voltage (V_{UC}). According to the control strategy in Figure 4, they generate current signals for the battery (I_{bat}^*) and UC (I_{UC}^*). Additionally, two current sensors measure the inductor currents i_{L1} and i_{L2} for both converters, providing feedback to minimize errors in reference currents. A voltage sensor for the DC link (V_{dc}) is used to maintain the DC-link voltage at 48 V. The conversion ratio of these current sensors is 1 A/1 mA. A 10 kHz switching frequency is used for the operation of the converters. Shared bus topology is used for the effective control of the performance indicators. Table 4 lists the components utilized in the hardware development.

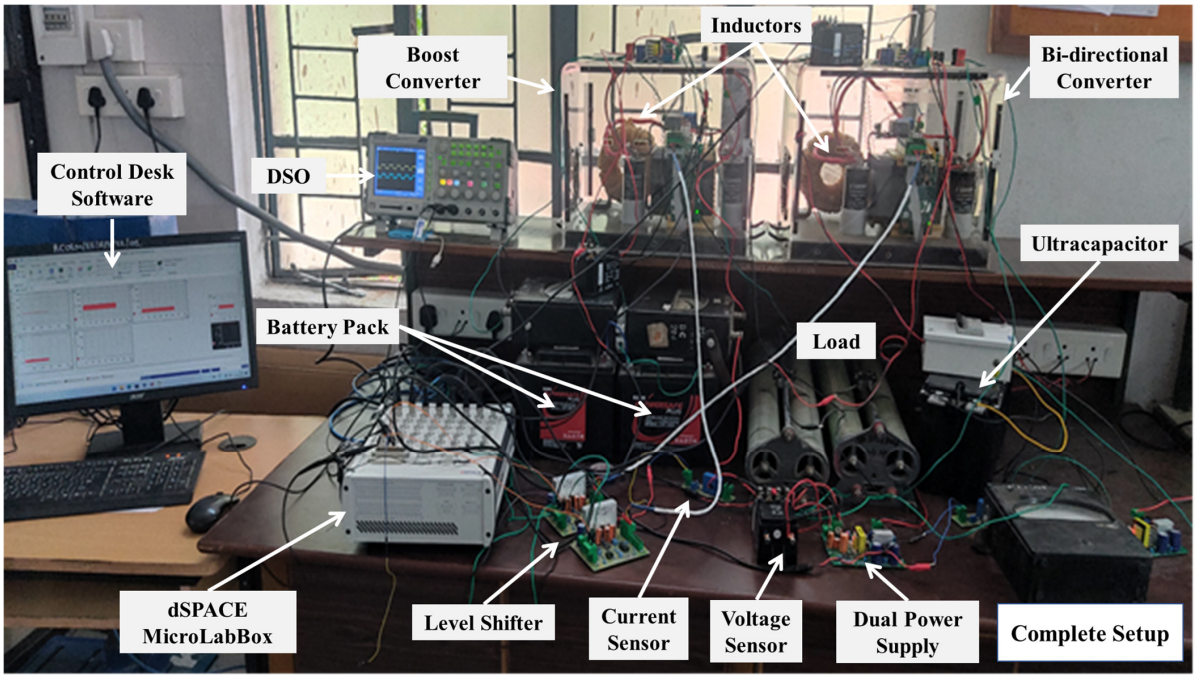

Figure 5. Experimental setup.

Table 4. Component ratings.

Sr. No	Component	Description	Unit
01	dSPACE MicroLabBox and auxiliary assembly	1. Highly efficient and high-speed controller	01
		2. Analog inputs crocodile pin	06
		3. Digital output pulse wire	02
		4. Level shifter (two outputs—3.3 V to 15 V)	01
		5. Dual power supply (±15 V)	04
		6. Current sensors (LA55P)	04
		7. Voltage transducers (LEM CV3-500)	03
02	Battery	12 V, 100 Ah battery	02
03	Ultracapacitor	24.3 V, 250 F	01
04	Converter module	1. Inductor—1.5 mH, 60 A	02
		2. IGBT module—Semikron, 75 A	02
		3. Output capacitor—3000 µF, 100 V	02
		4. Input capacitor—1200 µF, 50 V	02
05	Load	500 watts (resistive)	01

A variable resistor is used by keeping the DC-link voltage constant to achieve variable power. The operation of the converters is in boost mode.

The main concern in this verification model is the real-time power-sharing strategy for different load conditions. In this experiment, the base power selected is 70 watts. If the total load power requirement is below the base power, the battery will provide the power required by the load. If the power of the load needed is higher than the base power, then the UC will assist the battery with the increased load power, and both will satisfy the required load power. LPDM and HPDM are two different load conditions used for power-sharing verification.

6. Performance Analysis

In this section of the research work, the real-time output results are discussed in context with the power-sharing and DC-link voltage regulation. A comparative analysis of the results is performed on the results obtained on the basis of the power demanded mode.

6.1. Analysis for Low-Power Demand Mode

The pulses are generated in real time for both modes and are shown in Figure 6. In Figure 6a, the pulse is generated for switch Q_1 only because in LPDM, the battery alone operates. In Figure 6b, the pulses are generated for both switches Q_1 and Q_2 because of the high power demanded. Here, the UC supports the battery. The pulse frequency can be seen to be 10 kHz in real time on a digital oscilloscope. The DC-link voltage or load voltage (V_m) is shown in Figure 7. In Figure 7a,b, for low-power demand conditions, the DC-link voltage is approximately constant at 48 V for the simulated and experimental environment. The percentage of error between the experimental and Simulink results for the DC-link voltage is ±2.08%. ControlDesk software (version ControlDesk 7.4) is used to extract all the waveforms in a real-time environment. A voltage sensor captures the DC-link voltage at the load side. The LEM-CV3-500 voltage transducer is used for voltage measurement and its close-loop feedback. An internal loop is used for the compensation of the DC-link voltage and is shown in Figure 4 in the EMS section.

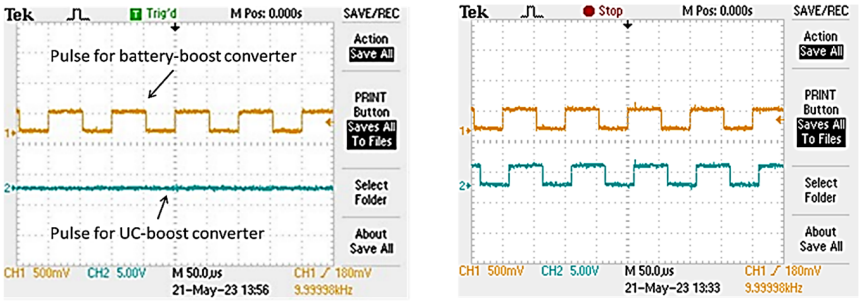

(**a**) (**b**)

Figure 6. Generated pulse for (**a**) a battery-boost converter (switch Q1) and (**b**) shared bus configuration (switches Q1 and Q2).

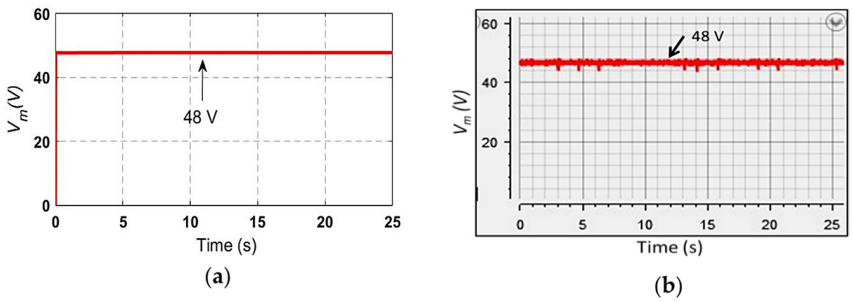

(**a**) (**b**)

Figure 7. Load voltage profile during LPDM for (**a**) simulation and (**b**) experimentation.

The load current (I_m) for LPDM is displayed in Figure 8. The load current is 0.93 A in the simulation environment for the power requirement of 47.2 watts, as shown in Figure 9. This simulated result closely matched with the experimental result, as shown in Figure 8b, which is 0.91 A for the same power requirement. The percentage error in the load current is ±2.1%. In order to capture the load current, a current sensor (LA55P) at the load side is used. Its conversion factor is used in the real-time interface of dSPACE Simulink.

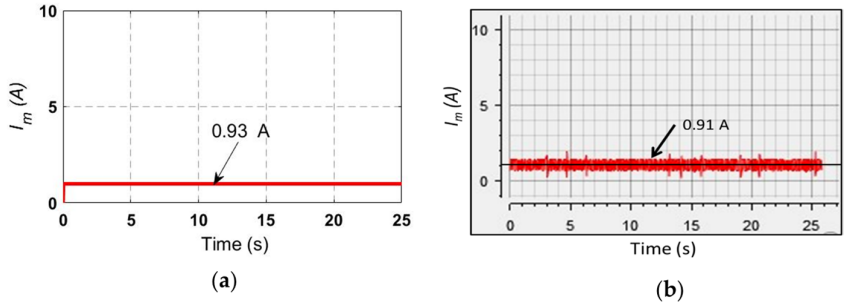

Figure 8. Load current profile during LPDM for (**a**) simulation and (**b**) experimentation.

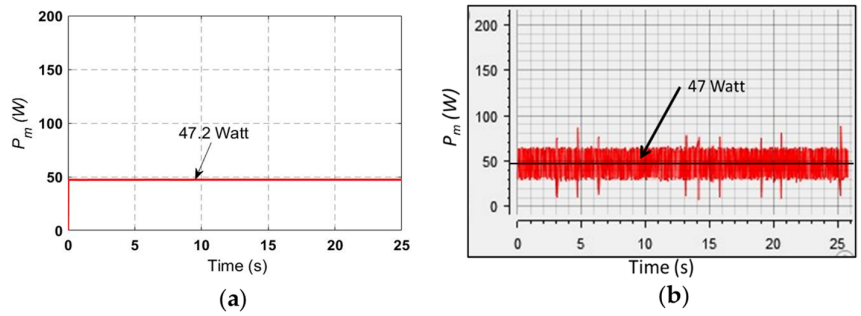

Figure 9. Load power profile during LPDM for (**a**) simulation and (**b**) experimentation.

The load power profile P_m for LPDM is shown in Figure 9. During simulation, the load power profile is 47.2 watts, as shown in Figure 9a, whereas during experimentation, the average power is 47 watts, as shown in Figure 9b. The percentage of error in the load power is approximately 5.6%. The base power selected is 70 watts. So, in LPDM, the load power required is 47.2 watts. This load requirement is completely fulfilled by the battery only, as shown in Figures 10a and 10b during simulation and experimental verification, respectively. The error in the battery power profile is 0.2%. In LPDM, the battery alone handles the load, and the contribution of the UC is negligible and is shown in Figures 11a and 10b during simulation and experimentation, respectively. The error in the UC power profile is almost zero percent.

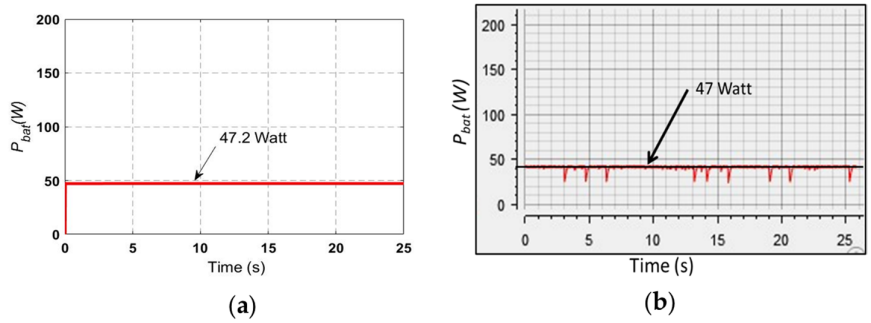

Figure 10. Battery power profile during LPDM for (**a**) simulation and (**b**) experimentation.

So, during the low-power demand mode, the proposed strategy is effective in allocating the power.

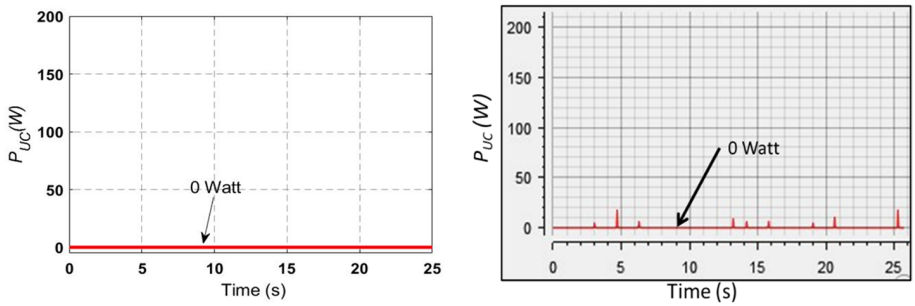

Figure 11. UC power profile during LPDM for (**a**) simulation and (**b**) experimentation.

6.2. Analysis for High-Power Demand Mode

After successful verification of the LPDM, it is time to validate the control strategy for the high-power demand mode (HPDM). In this mode, the total load power required is 78.6 watts during simulation. For this load, the DC-link voltage is constant at 48 V, as shown in Figure 12, for both the verification methods (simulation and experimental). To handle this load, the simulated load current is 1.9 A, which is very close to the experimental result, which is 1.96 A, as shown in Figures 13a and 13b, respectively. The battery handles only 70 watts of power out of 78.6 watts; the rest is carried out by the UC as per the proposed control strategy and is validated by the simulation and experimental results, as shown in Figures 14–16. As the UC assists the battery with the increased load power from its base power, the UC delivers 8.76 watts of power. The UC, being the high-power density, safeguards the battery from peak power demand. The selection of the UC rating is critical as it has to provide the increased load requirement.

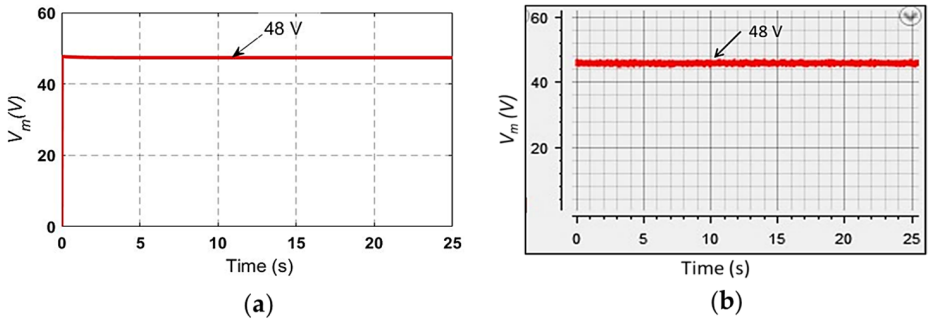

Figure 12. Load voltage profile during HPDM for (**a**) simulation and (**b**) experimentation.

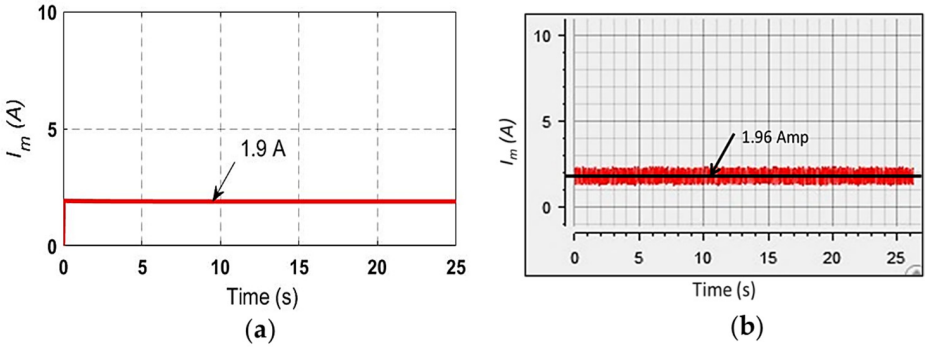

Figure 13. The load current profile during HPDM for (**a**) simulation and (**b**) experimentation.

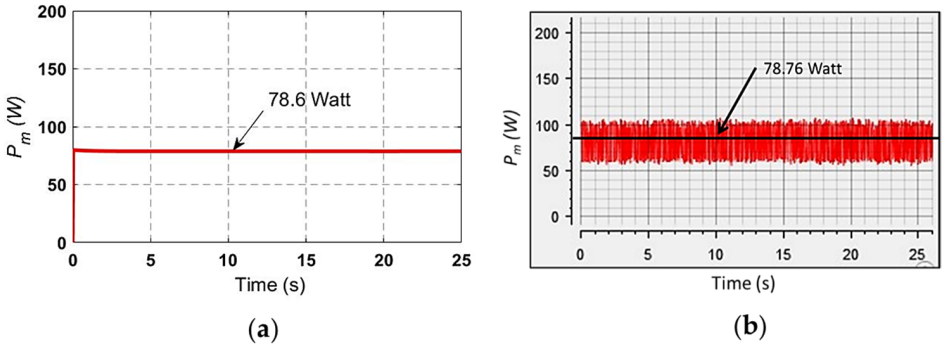

Figure 14. The load power profile during HPDM for (**a**) simulation and (**b**) experimentation.

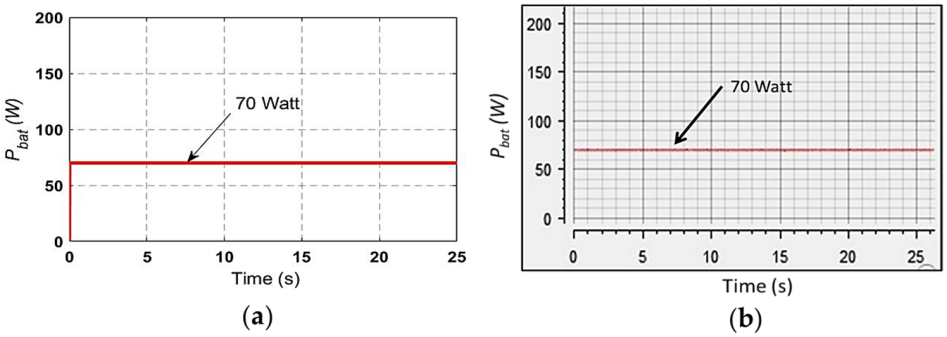

Figure 15. The battery power profile during HPDM for (**a**) simulation and (**b**) experimentation.

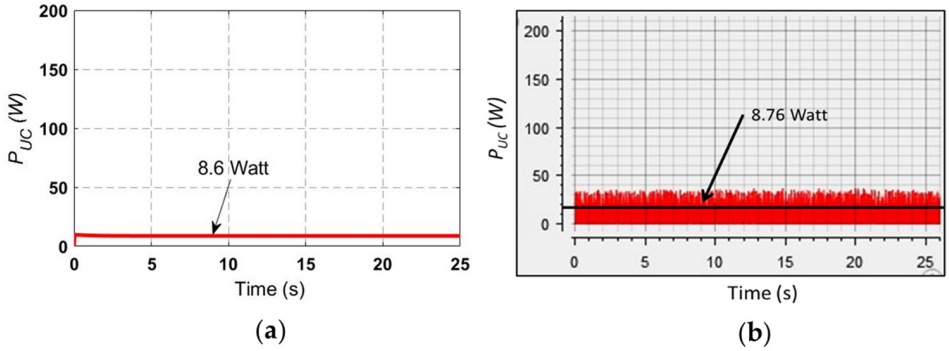

Figure 16. The UC power profile during HPDM for (**a**) simulation and (**b**) experimentation.

7. Conclusions

In this research work, an experimental study is carried out to analyze the power-sharing strategy and regulation of the DC-link voltage. A shared bus topology with modified EMS is used to verify the above indicators. The control strategy is developed in the dSPACE real-time interface (RTI) window. A dedicated RTI library is used for interfacing the hardware dSPACE MicroLabBox.

To create this control strategy in the real-time interface (RTI) window, signals from current and voltage sensors are connected to six analog pins. After processing these signals as per requirements, two pulses are generated for switches Q_1 and Q_2. The switching frequency for the pulse width modulation generation is 10 kHz. The designed rating of the converter module is 1.2 kW and has a load of 500 watts.

This experimentation is carried out for the two operational modes, LPDM and HPDM. The base power for this experiment is taken as 70 watts. The battery provides power only up to base power, and this strategy is also verified by experimentation. For high-power demand (87.78 watts), both sources should provide the power to the load in real time, and it is verified from the RTI waveform in Figures 14b and 16b. Irrespective of

the load conditions, the DC-link voltage is constant, as shown in the RTI waveform in Figures 7b and 12b.

From the experimental study, the proposed EMS proved its effectiveness in real time. The DC-link voltage regulation and power-sharing strategy are also verified. They can be employed in various applications, including electric vehicles and microgrids.

Author Contributions: Conceptualization, A.R. and S.B.; methodology, A.R., A.B. and G.G.; software, A.R. and S.B.; validation, A.R. and G.G.; formal analysis, S.B.; investigation, S.B.; resources, A.B.; data curation, S.T.; writing—original draft preparation, A.R.; writing—review and editing, A.R.; visualization, S.T.; supervision, S.B.; project administration, S.B.; funding acquisition, S.B. and G.G. All authors have read and agreed to the published version of the manuscript.

Funding: This work is supported by the All-India Council of Technical Education under the Research Promotion Scheme with Grant No. 8-206/FDC/RPS/(SC&ST)/POLICY-1/2021-22.

Data Availability Statement: The original contributions are included in the article; further enquiries can be directed to the first author.

Conflicts of Interest: The authors declare no conflicts of interest.

Nomenclatures

BEV	Battery electric vehicle
C_{bat}	Input capacitor
C_{dc}	DC-link capacitor
D	Duty cycle
DRAM	Dynamic random-access memory
d_{Q1}, d_{Q2}	Duty ratio for Q_1 and Q_2
EMS	Energy management strategy
$E_n(t)$	Expression of energy
F	Falling slew rate
FC	Fuel cell
f_s	Switching frequency
HESS	Hybrid energy storage system
HPDM	High-power demand mode
I_{bat}	Battery current
I_{bat}^*	Battery signal current
i_{L1}, i_{L2}	Inductor currents in converters
I_m	Load current
I_{out_max}	Maximum output current
I_{UC}	Ultracapacitor current
I_{UC}^*	UC signal current
L_1, L_2	Inductors
LPDM	Low-power demand mode
MRB-EMS	A modified rule-based EMS
P_{bat}	Power delivered by the battery
P_m	Required load power
P_{UC}	Power delivered by the UC
Q_0, Q_1, Q_2	Power switches
R	Rising slew rate
R_a	Load resistance
RTI	Real-time interface
SOC	State of charge
UC	Ultracapacitor
$U(P_{bat})$	Battery power at the current step
V_{bat}	Battery voltage
V_{dc}^*	DC-link signal
V_{in}	Input voltage
V_{in_min}	Minimum input voltage

V_{Out}	Desired output voltage
W_{UC}	The total energy required by the UC
$Y(P_{bat}-1)$	Battery power in the previous step
Δt	Sample time
ΔI_L	Ripple current in the inductor
ΔV_{out}	Ripple voltage

References

1. Sutikno, T.; Arsadiando, W.; Wangsupphaphol, A.; Yudhana, A.; Facta, M. A Review of Recent Advances on Hybrid Energy Storage System for Solar Photovoltaics Power Generation. *IEEE Access* **2022**, *10*, 42346–42364. [CrossRef]
2. Timilsina, L.; Badr, P.R.; Hoang, P.H.; Ozkan, G.; Papari, B.; Edrington, C.S. Battery Degradation in Electric and Hybrid Electric Vehicles: A Survey Study. *IEEE Access* **2023**, *11*, 42431–42462. [CrossRef]
3. Ranjith Kumar, R.; Bharatiraja, C.; Udhayakumar, K.; Devakirubakaran, S.; Sekar, K.S.; Mihet-Popa, L. Advances in Batteries, Battery Modeling, Battery Management System, Battery Thermal Management, SOC, SOH, and Charge/Discharge Characteristics in EV Applications. *IEEE Access* **2023**, *11*, 105761–105809. [CrossRef]
4. Ankar, S.J.; Pinkymol, K.P. Optimal Sizing and Energy Management of Electric Vehicle Hybrid Energy Storage Systems With Multi-Objective Optimization Criterion. *IEEE Trans. Veh. Technol.* **2024**, *73*, 11082–11096. [CrossRef]
5. Mohammad, J.S.S.; Bhanabhagvanwala, D. Simulation Analysis of Battery/Ultracapacitor Hybrid Energy Storage System for Electric Vehicle. In Proceedings of the 2019 International Conference on Intelligent Sustainable Systems (ICISS), Palladam, India, 21–22 February 2019; pp. 494–498. [CrossRef]
6. Etxandi-Santolaya, M.; Mora-Pous, A.; Canals Casals, L.; Corchero, C.; Eichman, J. Quantifying the Impact of Battery Degradation in Electric Vehicle Driving through Key Performance Indicators. *Batteries* **2024**, *10*, 103. [CrossRef]
7. Meng, X.; Mei, J.; Tang, X.; Jiang, J.; Sun, C.; Song, K. The Degradation Prediction of Proton Exchange Membrane Fuel Cell Performance Based on a Transformer Model. *Energies* **2024**, *17*, 3050. [CrossRef]
8. Tang, X.; Zhang, Y.; Xu, S. Experimental Study of PEM Fuel Cell Temperature Characteristic and Corresponding Automated Optimal Temperature Calibration Model. *Energy* **2023**, *283*, 128456. [CrossRef]
9. Xu, J.; Sun, C.; Ni, Y.; Lyu, C.; Wu, C.; Zhang, H.; Yang, Q.; Feng, F. Fast Identification of Micro-Health Parameters for Retired Batteries Based on a Simplified P2D Model by Using Padé Approximation. *Batteries* **2023**, *9*, 64. [CrossRef]
10. Tang, X.; Shi, L.; Zhang, Y.; Li, B.; Xu, S.; Song, Z. Degradation Adaptive Energy Management Strategy for FCHEV Based on the Rule-DDPG Method: Tailored to the Current SOH of the Powertrain. *IEEE Trans. Transp. Electrif.* **2024**, 1. [CrossRef]
11. Zhang, R.; Li, X.; Sun, C.; Yang, S.; Tian, Y.; Tian, J. State of Charge and Temperature Joint Estimation Based on Ultrasonic Reflection Waves for Lithium-Ion Battery Applications. *Batteries* **2023**, *9*, 335. [CrossRef]
12. Naseri, F.; Farjah, E.; Ghanbari, T. An Efficient Regenerative Braking System Based on Battery/Supercapacitor for Electric, Hybrid, and Plug-in Hybrid Electric Vehicles with BLDC Motor. *IEEE Trans. Veh. Technol.* **2017**, *66*, 3724–3738. [CrossRef]
13. Garg, R.; Yadav, K.; Babber, A.; Jaggi, A.; Sharma, A.; Bijlwan, S. Energy Storage System Analysis Based on State of Charge for Hybrid Electric Vehicle. In Proceedings of the 2023 9th International Conference on Smart Computing and Communications: Intelligent Technologies and Applications, ICSCC, Kochi, India, 17–19 August 2023.
14. Zhang, Q.; Wang, L.; Li, G.; Liu, Y. A Real-Time Energy Management Control Strategy for Battery and Supercapacitor Hybrid Energy Storage Systems of Pure Electric Vehicles. *J. Energy Storage* **2020**, *31*, 101721. [CrossRef]
15. Zahedi, A.; Babaeiyazdi, I.; Ostadian, R.; Rezaei-Zare, A. Globally Optimal Energy Management in a Battery-Ultracapacitor Electric Vehicle. In Proceedings of the 2022 IEEE International Conference on Environment and Electrical Engineering and 2022 IEEE Industrial and Commercial Power Systems Europe (EEEIC/I and CPS Europe), Prague, Czech Republic, 28 June–1 July 2022.
16. Choudhary, M.K.; Sharma, A.K. Integration of PV, Battery and Supercapacitor in Islanded Microgrid. In Proceedings of the 2020 International Conference on Emerging Frontiers in Electrical and Electronic Technologies (ICEFEET), Patna, India, 10–11 July 2020. [CrossRef]
17. Reddy, R.M.; Das, M.; Chauhan, N. Novel Battery-Supercapacitor Hybrid Energy Storage System for Wide Ambient Temperature Electric Vehicles Operation. *IEEE Trans. Circuits Syst. II Express Briefs* **2023**, *70*, 2580–2584. [CrossRef]
18. Sidorov, D.; Muftahov, I.; Tomin, N.; Karamov, D.; Panasetsky, D.; Dreglea, A.; Liu, F.; Foley, A. A Dynamic Analysis of Energy Storage with Renewable and Diesel Generation Using Volterra Equations. *IEEE Trans. Ind. Inform.* **2020**, *16*, 3451–3459. [CrossRef]
19. Karamov, D.N.; Muftahov, I.R. Mathematical Modeling of Battery Energy Storage System Operating Modes Using Volterra Integral Equations. *Vestn. IzhGTU Im. M.T. Kalashnikova* **2022**, *25*, 92–99. [CrossRef]
20. Ostadian, R.; Ramoul, J.; Biswas, A.; Emadi, A. Intelligent Energy Management Systems for Electrified Vehicles: Current Status, Challenges, and Emerging Trends. *IEEE Open J. Veh. Technol.* **2020**, *1*, 279–295. [CrossRef]
21. Jarraya, I.; Abdelhedi, F.; Rizoug, N. An Innovative Power Management Strategy for Hybrid Battery–Supercapacitor Systems in Electric Vehicle. *Mathematics* **2024**, *12*, 50. [CrossRef]
22. Hosseini, S.M.; Soleymani, M.; Kelouwani, S.; Amamou, A.A. Energy Recovery and Energy Harvesting in Electric and Fuel Cell Vehicles, a Review of Recent Advances. *IEEE Access* **2023**, *11*, 83107–83135. [CrossRef]

23. Modu, B.; Abdullah, M.P.B.; Alkassem, A.; Garni, H.Z.A.; Alkabi, M. Optimal Design of a Grid-Independent Solar-Fuel Cell-Biomass Energy System Using an Enhanced Salp Swarm Algorithm Considering Rule-Based Energy Management Strategy. *IEEE Access* **2024**, *12*, 23914–23929. [CrossRef]
24. Ravada, B.R.; Tummuru, N.R. Control of a Supercapacitor-Battery-PV Based Stand-Alone DC-Microgrid. *IEEE Trans. Energy Convers.* **2020**, *35*, 1268–1277. [CrossRef]
25. Djilali, A.B.; Yahdou, A.; Bounadja, E.; Benbouhenni, H.; Zellouma, D.; Colak, I. Energy Management of the Hybrid Power System Based on Improved Intelligent Perturb and Observe Control Using Battery Storage Systems. *Energy Rep.* **2024**, *11*, 1611–1626. [CrossRef]
26. Li, H.; Liu, Z.; Yang, Y.; Yang, H.; Shu, B.; Liu, W. A Proactive Energy Management Strategy for Battery-Powered Autonomous Systems. *Appl. Energy* **2024**, *363*, 122995. [CrossRef]
27. Han, Y.; Xie, X.; Deng, H.; Ma, W. Central Energy Management Method for Photovoltaic DC Micro-Grid System Based on Power Tracking Control. *IET Renew. Power Gener.* **2017**, *11*, 1138–1147. [CrossRef]
28. Abeywardana, D.B.W.; Hredzak, B.; Agelidis, V.G.; Demetriades, G.D. Supercapacitor Sizing Method for Energy-Controlled Filter-Based Hybrid Energy Storage Systems. *IEEE Trans. Power Electron.* **2017**, *32*, 1626–1637. [CrossRef]
29. Zhang, Q.; Deng, W.; Zhang, S.; Wu, J. A Rule Based Energy Management System of Experimental Battery/Supercapacitor Hybrid Energy Storage System for Electric Vehicles. *J. Control Sci. Eng.* **2016**, *2016*, 18–20. [CrossRef]
30. Akar, F.; Tavlasoglu, Y.; Vural, B. An Energy Management Strategy for a Concept Battery/Ultracapacitor Electric Vehicle with Improved Battery Life. *IEEE Trans. Transp. Electrif.* **2017**, *3*, 191–200. [CrossRef]
31. Trovao, J.P.F.; Roux, M.A.; Menard, E.; Dubois, M.R. Energy- and Power-Split Management of Dual Energy Storage System for a Three-Wheel Electric Vehicle. *IEEE Trans. Veh. Technol.* **2017**, *66*, 5540–5550. [CrossRef]
32. Sellali, M.; Betka, A.; Drid, S.; Djerdir, A.; Malik, O.P. Hardware Implementation of an Improved Control Strategy for Battery–Supercapacitor Hybrid System in Electric Vehicles. *IET Electr. Syst. Transp.* **2020**, *10*, 204–212. [CrossRef]
33. Raveendhra, D.; Poojitha, R.; Narasimharaju, B.L.; Domyshev, A.; Dreglea, A.; Dao, M.H.; Pathak, M.; Liu, F.; Sidorov, D. Part II: State-of-the-Art Technologies of Solar-Powered DC Microgrid with Hybrid Energy Storage Systems: Converter Topologies. *Energies* **2023**, *16*, 6194. [CrossRef]
34. Ranjan, A.; Bodkhe, S.B. Energy Management Strategy for Hybrid Energy Storage Systems in Electric Vehicle—A Review. *Int. J. Electr. Electron. Eng. Telecommun.* **2022**, *11*, 88–101. [CrossRef]
35. Al Takrouri, M.; Md Ayob, S.; Nik Idris, N.R.; Aziz, M.J.A.; Ayop, R.; Said, M.F.B.M. Comparative Analysis of Passive and Semi-Active Hybrid Energy Storage System Topologies for Electric Vehicle. In Proceedings of the 2023 IEEE Conference on Energy Conversion, CENCON, Kuching, Malaysia, 23–24 October 2023.
36. Badawy, M.O.; Husain, T.; Sozer, Y.; De Abreu-Garcia, J.A. Integrated Control of an IPM Motor Drive and a Novel Hybrid Energy Storage System for Electric Vehicles. *IEEE Trans. Ind. Appl.* **2017**, *53*, 5810–5819. [CrossRef]
37. Fathabadi, H. Plug-In Hybrid Electric Vehicles: Replacing Internal Combustion Engine with Clean and Renewable Energy Based Auxiliary Power Sources. *IEEE Trans. Power Electron.* **2018**, *33*, 9611–9618. [CrossRef]
38. Gan, C.; Jin, N.; Sun, Q.; Kong, W.; Hu, Y.; Tolbert, L.M. Multiport Bidirectional SRM Drives for Solar-Assisted Hybrid Electric Bus Powertrain with Flexible Driving and Self-Charging Functions. *IEEE Trans. Power Electron.* **2018**, *33*, 8231–8245. [CrossRef]
39. RANJAN, A.; BODKHE, S.B.; GOYAL, G.N.; AWARE, M.V. Heuristics EMS for HESS of Electric Vehicle to Extended Battery Operation Using Rate Limiter. *Adv. Electr. Comput. Eng.* **2022**, *22*, 11–22. [CrossRef]
40. Denis, N.; Dubois, M.R.; Trovao, J.P.F.; Desrochers, A. Power Split Strategy Optimization of a Plug-in Parallel Hybrid Electric Vehicle. *IEEE Trans. Veh. Technol.* **2018**, *67*, 315–326. [CrossRef]
41. Singh, A.; Pattnaik, S. Design of a Efficient Power Sharing Strategy for a Battery-Ultracapacitor Hybrid Energy Storage System. In Proceedings of the 2016 IEEE 1st International Conference on Power Electronics, Intelligent Control and Energy Systems (ICPEICES), Delhi, India, 4–6 July 2016. [CrossRef]
42. Ranjan, A. Hybrid Energy Storage System for Electric Vehicle. *Helix* **2019**, *9*, 5801–5805. [CrossRef]
43. Ranjan, A.; Bodkhe, S.B. Modified Energy Management Strategy for HESS in Electric Vehicle. In Proceedings of the 2021 9th IEEE International Conference on Power Systems (ICPS), Kharagpur, India, 16–18 December 2021; IEEE: Piscateville, NJ, USA, 2021; pp. 1–6.
44. Ranjan, A.; Bodkhe, S.B. Fuzzy Logic Controller Based Modified Energy Management Strategy for Battery and UC with Improved Battery Performance. *ECS Trans.* **2022**, *107*, 2457–2469. [CrossRef]
45. Wong, D.; Shrestha, B.; Wetz, D.A.; Heinzel, J.M. Impact of High Rate Discharge on the Aging of Lithium Nickel Cobalt Aluminum Oxide Batteries. *J. Power Sources* **2015**, *280*, 363–372. [CrossRef]
46. Hauke, B. *Basic Calculation of a Boost Converter's Power Stage*; Application Report November; Texas Instruments: Dallas, TX, USA, 2009; pp. 1–9.
47. MicroLabBox MicroLabBox. 2020, 1–12. Available online: https://www.dspace.com/shared/data/pdf/2020/dSPACE-MicroLabBox_Product-Brochure_2020-01_EN.pdf (accessed on 1 November 2024).